# Photocatalytic Degradation Dynamics of Methyl Orange Using Coprecipitation Synthesized $Fe_3O_4$ Nanoparticles

Yousef Al-Abdallat · Inshad Jum'h · Abeer Al Bsoul ·
Rami Jumah · Ahmad Telfah

**Abstract** This study aims to investigate the photocatalytic degradation performance, mechanism, and dynamics of methyl orange (MO) which is a widely used organic dye in textile industries as well a hazardous wastewater pollutant. The degradation process was catalyzed by employing a synthesized $Fe_3O_4$ magnetic nanoparticle (NP) using the coprecipitation method. The structural and morphological properties of the synthesized $Fe_3O_4$ NPs were investigated by employing XRD, HR-SEM, and XPS, which proved that acquired $Fe_3O_4$ NPs were in a pure phase. Moreover, the crystallite sizes fall in the range of 28–31.8 nm and were estimated by applying the Scherrer equation on the XRD spectrum as well as calculated independently by applying a statistical approach on the SEM micrographs. The UV–Vis maximum in the visible range at 468.8 nm consists of two absorption frequency bands due to the effect of the hydrogen-bond interaction between water and the azo nitrogens in the MO. A non-monotonic spectral dynamic accompanied by peak wavelength shifts, as well as the absolute signal amplitude and signal area of the MO band, suggests that a cleavage of the azo bond is not the only and/or the dominant process in the photocatalytic oxidization of the MO in a protic solvent. The overall absorbance process is a complicated response to a combination of nonspecific and specific solute-solvent interactions, dipole-dipole interactions, hydrogen-bonding networks, and other possible intermolecular interactions such as hydrophobic/hydrophilic interactions. A bi-exponential decay was found to be the best fitting function to model the decay of the time-dependent electrical conductivity of the MO aqueous solution under photocatalytic oxidization. The $Fe_3O_4$ NPs exhibited a 98.3% removal of MO within 110 min. Photocatalytic degradation of methyl orange can be modeled to the first-order model with a rate constant $k$ of 0.037 $min^{-1}$ taking into account the initial concentration of 1175 ppm of MO. The degradation/

Y. Al-Abdallat
Industrial Engineering Department, School of Engineering, The National Program for Linkage Academic Institutions with Industrial Sectors "Faculty for Factory FFF", The University of Jordan (UJ), Amman 11942, Jordan

I. Jum'h
School of Basic Sciences and Humanities, German-Jordanian University (GJU), Amman 11180, Jordan

A. Al Bsoul
Department of Chemical Engineering, Al-Huson University College, Al-Balqa Applied University, P.O. Box 50, Al-Huson, Irbid, Jordan

R. Jumah
Department of Chemical Engineering, Jordan University of Science and Technology, Irbid 22110, Jordan

A. Telfah
Leibniz-Institut für Analytische Wissenschaften - ISAS - e.V., 44139 Dortmund, Germany

A. Telfah (✉)
Hamdi Mango Center for Scientific Research (HMCSR), The University of Jordan (UJ), Amman 11942, Jordan
e-mail: telfah.ahmad@isas.de

decolorization efficiency deduced from the low-frequency band of the visible spectra is around 99.4% after 110 min. The real-time degradation/decolorization efficiencies deduced from the overall absorbance maxima and the low-frequency band have a discrepancy of 50.1% at 20 min and 12.3% at 60 min representing the progressive attenuation of the H-bond impact dissociation of MO (degradation/decolorization).

**Keywords** $Fe_3O_4$ nanoparticles · Methyl orange · Photocatalytic degradation · Organic pollutant · Textile industries wastewater · Hydrogen bond · Hydrophobic–hydrophilic interaction

## 1 Introduction

The disposal of the textile industry wastewater is one of the most important environmental problems since it is commonly contains large amount of organic chemicals described by low biodegradability, dyes, and salinity (Yaseen and Scholz 2019; Tzitzi et al. 1994).

Dyes are colored substances and highly soluble chemical compounds widely used in the textile industry for coloring the textile tissues. The direct discharge of concentrated dye solutions can contaminate water resources with hazardous substances, since dyes prevent solar light penetration and ultimately reduce photosynthesis processes of aquatic plants and organisms (Alinsafi et al. 2007). Moreover, dyes such as methyl orange (MO), which is a chemical indicator used regularly used in acid-base titrations for standardization of solutions and alkalinity determination, has mutagenic properties (Silva et al. 2017) and is a non-biodegradable sulfonated azo dye (Lau et al. 2015).

Reusing industrial wastewater has promising economic potentials for the industrial sectors and is an important strategy for reducing freshwater consumption and for environmental pollution control (Barbosa et al. 2018). Hence, the impact of the textile wastewater effluent on the environment was studied extensively in the past decades not only for the disposal of pollutants but also for the consumption of water and energy (Sauer et al. 2002). Different individual and combined treatments have been developed for industrial wastewater treatment, for instance adsorption (Rizzo et al. 2019), flocculation, and advanced oxidation processes such as ultraviolet photolysis and photocatalytic degradation (Jum'h et al. 2017a; Pacheco-Álvarez et al. 2018a).

The nanoparticle technology applications in solving environmental problems have received considerable attention due to their greater efficiency in decontamination of the recalcitrant pollutants (Mortazavian et al. 2019) as well as their low cost and their reduced environmental toxicity (Genuino et al. 2013; Guerra et al. 2017). The combination treatments of wastewater by employing the photocatalytic degradation processes and nanoparticle technology are gaining importance since they result in a complete mineralization with operation under natural weathering conditions (Legrini et al. 1993; Lops et al. 2019).

Magnetic iron oxide nanoparticles ($Fe_3O_4$ NPs) are being employed for wastewater treatment in the absorption of arsenite, arsenate, chrome, cadmium, and nickel (Bagbi et al. 2017; Xin et al. 2012) and in organic compounds removal (Gutierrez et al. 2017). The concept of rational designing of $Fe_3O_4$ NPs for water treatment is to control physicochemical properties such as particle size, surface characteristic, and surfactants (surface active agents) in order to achieve the site-specific action of the ion exchange (Heidari et al. 2016). Small size nanoparticles have a tendency to aggregate (Guo et al. 2018) giving rise to considerable difficulties in physical handling in liquid and dry forms, which have to be overwhelmed before it can be used in water treatment.

This study reports the investigation of the degradation/decolorization of MO (Fig. 1(Nançoz et al. 2018)), which belongs to the push–pull azobenzenes (pp-ABs) family that are among the molecules whose excited state dynamics are the most investigated.

Despite MO is commonly used as a pH indicator and widely a model for organic environmental contaminants (Alqaradawi and Salman 2002; Dagher et al. 2018); its physicochemical properties have not been thoroughly investigated. The real-time dynamics of the formed hydrogen bonded in water–water–MO are investigated using a combination of UV irradiation and synthesized $Fe_3O_4$ NPs. The UV–Vis absorption spectra in addition to the spectral shape and quantitative calculations reveal essential information regarding the system dynamics including the H-bond, proton carriers, and acidity evolution. H-bond interactions have been found to affect the nature of the excited state app-Abs (Nançoz et al. 2018) (MO belong to app-Abs), but their effect on the MO photo-oxidation dynamics has not been methodically investigated.

In this study, overall dynamics of long and short distance H-bond networks together with the

hydrophobicity effect on MO photo-oxidization/decolorization effectiveness has been quantitatively calculated based on the peak advancement of the experimental UV–Vis spectra.

Besides, water polluted synthetically with MO was treated using the photodegradation technique catalyzed with the synthesized $Fe_3O_4$ NPs by the coprecipitation method demonstrating the efficiency of this process once the proper synthesize $Fe_3O_4$ NPs is attained.

Water is a very structured solvent, although it interacts strongly with organic molecules and dissociated ions (Eisenberg and Kauzmann 1969). H-bonding influence in the photodegradation of organic pollutants has not been appropriately explicated and particularly once the acidity is not controlled. Small organic molecules such as MO are miscible in water forming H-bond with water molecules leading to disrupt the water–water H-bonding networks (Dannenberg 2002; Alavi et al. 2010; Laage and Hynes 2006). The hydroxyl groups that are generated during the photodegradation process act as proton acceptors and proton donors at the same time; therefore, there is a large probability of instantaneous hydrogen bonding between O and H hydroxyl atoms with different water molecules (Alavi et al. 2010). Usually, MO and other small molecules are in solvents with lower polarity and hydrogen-bonding capabilities and therefore interact less with the solute and are unlikely to form a very compact structure (Nardo et al. 2008). Hydrophobicity is a well-known phenomenon and it plays a crucial role in many chemical, biological, and environmental processes (Chandler 2005). The lack of H-bonding between water molecules and a substance often defines a hydrophobic interface (Jum'h et al. 2017b).
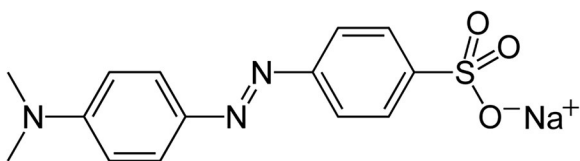


**Fig. 1** Chemical structure of methyl orange (MO). Linear formula is $C_{14}H_{14}N_3NaO_3S$

## 2 Experimental Details

### 2.1 Synthesis of Magnetite Nanoparticles

The $Fe_3O_4$ NPs have been synthesized using the coprecipitation method, and the size, shape, and crystallinity were attained depending on the synthesis conditions such as starting molar concentration, temperature reaction, the pH value, the stirring rate, and ionic strength of the buffer media.

A solution mixture of ferric chloride hexahydrate ($FeCl_3 \cdot 6H_2O$) and ferrous chloride tetrahydrate ($FeCl_2 \cdot 4H_2O$) salts with the addition to a base, namely ammonium hydroxide ($NH_4OH$), were prepared at room temperature. The first solution was prepared by dissolving 1 g of $FeCl_2 \cdot 6H_2O$ in hydrochloric acid (HCl) (2.5 mL of 1 M). The second solution was prepared by dissolving 2.7 g of $FeCl_3 \cdot 6H_2O$ in 25 mL deionized water and then added to HCl (10 mL of 1 M). The first and the second solutions were mixed and then $NH_4OH$ (20 mL, 25%) was added quickly under vigorous stirring. The precipitation process occurred immediately promoting a color change to dark black that is characteristic of the magnetite. The solution acidity (pH) was repetitively monitored and regulated to be in the range between 7 and 8 by washing several times with deionized water (Wu et al. 2011). After 30 min, 5 mL of tetramethylammonium hydroxide (TMAOH) $C_4H_{13}NO$ was added to the mixture, which works as a liquid carrier to modify the $Fe_3O_4$ NPs as well as to chemically stabilize the magnetic nanoparticles in a colloidal suspension. Moreover, TMAOH acts as a surfactant to nanoparticles by absorbing the cationic species at the surface OH groups thus creating an electrostatic repulsion layer surrounding the particles preventing the aggregation (Andrade et al. 2012) Additionally, it plays a key role in controlling the rates of nucleation and the growth rate that controls the final size (Lopez et al. 2010; Lacroix et al. 2013). Finally, the $Fe_3O_4$ NPs are washed with distilled water and then dried at room temperature in a vacuum oven for 24 h.

### 2.2 Characterization of Magnetic Nanoparticles

The size and the morphology of the synthesized $Fe_3O_4$ NPs were examined by direct observation via scanning electron microscopy (SEM). Additionally, X-ray photoelectron spectroscopy (XPS) was employed to better

characterize the phase and composition of the prepared $Fe_3O_4$ NPs.

The electrical conductivity and the acidity measurements were conducted with the use of a calibrated conductivity meter (Tintometer-Lovibond-Germany) and Mettler Toledo™ FiveEasy™ F20 pH/mV meters. Both measurements were conducted in a "real-time" frame enabling to correlate pH, COD, and UV–Vis results.

The crystallite sizes and the types of the synthesized $Fe_3O_4$ NPs were elucidated by employing X-ray diffraction (XRD) technique using (Philips X Pert, CuKα, around 43 kV, and $k = 1.54056$ Å) as described in (El Ghandoor et al. 2012). The XRD data were collected between $10° < 2θ < 85°$ using the CuKα radiation filtered in step scanning mode.

## 2.3 Photocatalytic Degradation Measurements of MO

An amount of 500 mL of MO aqueous solution that contains 10 mg of $Fe_3O_4$ NPs catalyst was placed in a batch reactor at ambient temperature in dark conditions for 30 min with continuous stirring for an adsorption/desorption equilibrium. Afterwards, the solution was exposed to UV irradiation using a low-pressure UV lamp (germicidal lamp, 4 W) with a wavelength peak at 254-nm emission. The distance between the surface of the solution and the light source was set to 10 cm. Later on, the aqueous solution was irradiated with UV–Vis light and the UV–Vis spectra were acquired and recorded with the help of the UV–Vis spectrometer (Perkin-Elmer 550 SE) at 465 nm; the measurement was conducted every 5 min at ambient temperature (nominally at room temperature). The chemical oxygen demand (COD) experimental values of treated samples were acquired using the dichromate standard method. Each sample was introduced into a commercially available digestion solution containing potassium dichromate (Hach-Germany), afterwards; the solution was incubated in a COD reactor (Hach Lange GmbH-Germany) for 120 min at 148 °C. The COD measurements were conducted using a spectrophotometer (DR Lange Lasa 100 Germany). Electrical conductivity (σ) and pH were measured using a Jenway 3540 pH/conductivity meter. Finally, the magnetic nanoparticles were collected using a rare earth permanent magnetic.

# 3 Results and Discussion

## 3.1 Characterization of $Fe_3O_4$ NPs

### 3.1.1 XRD Analysis of $Fe_3O_4$ NPs

The crystallinity of $Fe_3O_4$ NPs was investigated by employing XRD and results are shown in Fig. 2. The peaks in the $Fe_3O_4$ NPs XRD spectrum are observed at [111], [220], [311], [400], [422], [511], [620], [533], [622], and [440]. It may be noted the sites and intensity of the diffraction peaks are consistent with the standard pattern for JCPDS Card No. (79 - 0417) magnetite synthetic and with reported literatures on $Fe_3O_4$ NPs (Zysler et al. 2004; Namanga et al. 2013).

XRD peaks broadening reflecting the small crystalline size of the $Fe_3O_4$ NPs. The patterns of cube-like $Fe_3O_4$ NPs are observed in Fig. 2. Since the diffraction peaks correspond to the [111], [311], [222], [400], [422], [511], and [440], planes are observed, indicating the pure cubic phase of the $Fe_3O_4$ NPs. The sharp peaks indicate the high crystallinity of the $Fe_3O_4$ NPs. No impurity peaks have been detected indicating the synthesis method was pure and proper.

The crystallite sizes ($d_c$) of the synthesized $Fe_3O_4$ NPs have been estimated by the Scherrer formula using the average of all of XRD peaks (Sun and Zheng 2002) and the average size was 28 nm which is in good agreement with relevant reported literature for $Fe_3O_4$ NPs (Park et al. 2008; Mascolo et al. 2013). The average size distributions were calculated statistically by directly measuring the diameters of ensembles of nanoparticles in a single SEM micrograph and found to be around 31.5 nm (details are in Section 3.1.2).

### 3.1.2 SEM-EDAX Analysis of the $Fe_3O_4$ NPs

The SEM-EDAX results are demonstrated in Figs. 3 and 4. The $Fe_3O_4$ NPs are spherical in shape with sizes distributions falling in the range from 20 to 50 nm based on the direct observation of the SEM micrograph and direct size analysis. The size distributions were calculated statistically by measuring the diameters of more than a hundred of randomly selected $Fe_3O_4$ NPs that are in an SEM micrograph and are considered narrow. A spherical shape combined with a small size range and a narrow distribution is an advantage for efficient catalytic oxidization or electrochemical reactions (Jang et al. 2019; Ali et al. 2016).
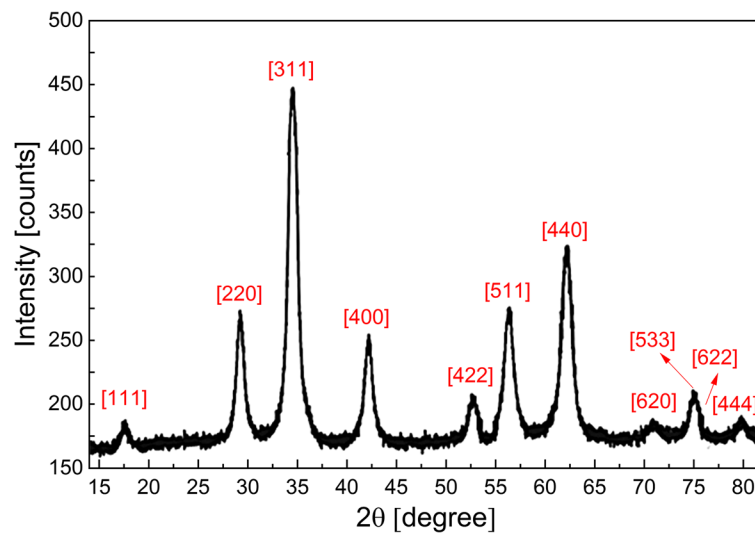
**Fig. 2** The XRD pattern of the synthesized $Fe_3O_4$ NPs

The EDAX analysis illustrates the elemental factor of the $Fe_3O_4$ NPs. Strong peaks referred to Fe and O atoms are observed in the spectrum with weight percentages of 81.84% and 17.32% respectively.

Traces of Cl as impurities remaining from the synthesis are about 0.84% (details are in Fig. 3) which are residual impurities of the starting materials since the ferric chloride hexahydrate ($FeCl_3 \cdot 6H_2O$) salt was one of the materials used in synthesizing $Fe_3O_4$ NPs. Further evidence of the existence of $FeCl_3 \cdot 6H_2O$ impurities is the existence of the absorbance peaks in the UV–Vis spectra.

### 3.1.3 XPS Analysis of $Fe_3O_4$ NPs

XPS have been employed to precisely identify the composition and the phase of the synthesized $Fe_3O_4$ NPs. Structural data presented in Fig. 5 illustrate the phase purity of the synthesized iron oxide samples.

Figure 5 shows the Fe 2p and O 1s X-ray photoemission spectra which reveal two peaks at ca. 711.1 and 726 eV which are attributed to the Fe $2p_{3/2}$ and Fe $2p_{1/2}$, respectively, indicating that the Fe is dominantly present as $Fe_3O_4$. Furthermore, the presence of satellite peaks around 719 eV, which is characteristic of $Fe_2O_3$ phases,
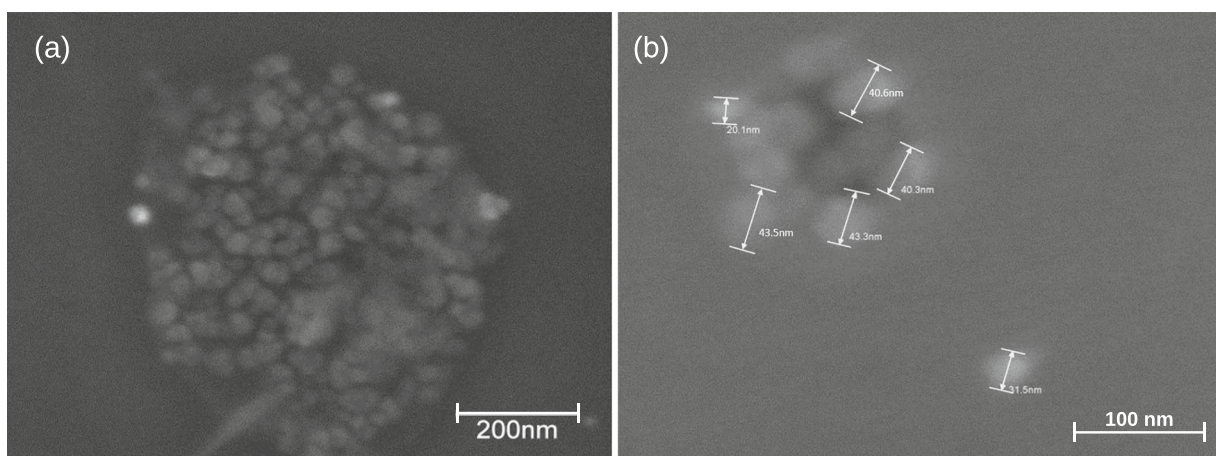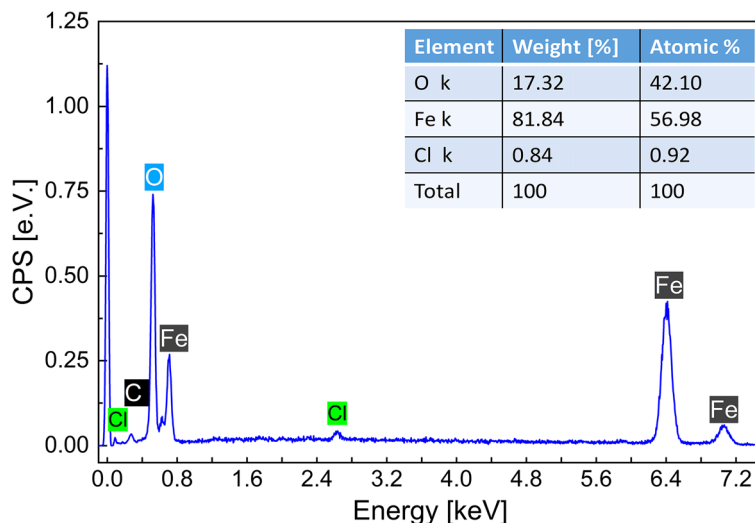


**Fig. 3** **(a)** SEM micrograph of the synthesized $Fe_3O_4$ NPs and **(b)** the enlarged and annotated SEM micrographs of the $Fe_3O_4$ NPs emphasizing the spherical shape and showing the size distributions

**Fig. 4** EDAX spectrum of the synthesized $Fe_3O_4$ NPs showing the elemental factors



| Element | Weight [%] | Atomic % |
|---------|-----------|----------|
| O k | 17.32 | 42.10 |
| Fe k | 81.84 | 56.98 |
| Cl k | 0.84 | 0.92 |
| Total | 100 | 100 |

confirms the presence of only $Fe^{3+}$ species in the lattice (Fujii et al. 1999; Ibrahim Dar and Shivashankar 2014).

Moreover, the O 1s core-level peak is characterized at ca. 531.1 eV that can be attributed to an Fe–O bond in the magnetite phase. XPS results emphasizing that only structural phase present in the synthesized nanoparticles is the $Fe_3O_4$ form. The atomic ratio of iron to oxygen (Fe:O = 1.33 for magnetite) confirms that a single-phase magnetite for the prepared NPs is dominantly present.

3.2 Photocatalytic Activity of the Synthesized $Fe_3O_4$ NPs

UV light illumination begins after 30 min of adsorption in the dark. Figure 6 shows the time-dependent photocatalytic degradation of MO.

The major absorption maxima of MO in the visible range is at 468.8 nm and in the UV range is at 265 nm at the start of the measurements. These two maxima disappeared completely after 110 min of irradiation indicating the complete decolorization of MO. The time evolution of the UV–Vis absorbance spectra (Fig. 6) does not seem to indicate simply a consecutive attenuation in the absorbance maxima with increasing irradiation time. Prominently, these maxima consist of more than a single absorption peak (frequency band). If the experimental absorption curve was a single peak, then the longer exposure of irradiation should merely have decreased the amplitude and have slightly increased the absorbance linewidth. Consequently, the observed change in the spectral configuration confirms the

presence of two absorbance frequency bands with peaks, which are affected differently by changing irradiation time. Additional evidence for the presence of two bands comes from the fact that an obvious shoulder is seen on the high-frequency side (around 398.3 nm) of the absorbance curve.

The peak at 662.2 nm is most likely associated with the impurities comes from the starting materials used in synthesizing $Fe_3O_4$ NPs since the ferric chloride hexahydrate ($FeCl_3 \cdot 6H_2O$) and ferrous chloride tetrahydrate ($FeCl_2 \cdot 4H_2O$) salts have absorption peaks in the range 620–670 nm (Bauer et al. 2005).

Further spectral analysis to quantify the low- and high-frequency absorbance bands of the visible spectrum of the MO over the irradiation time has been conducted. Interestingly, a significant and non-monotonic spectral dynamic including peak wavelength shifts, absolute amplitude, and area changes for the MO band (Fig. 8a–c) and probably for $Fe_3O_4$/MO complexes suggests the cleavage of an azo bond is not the only or the dominant process in the scenario. To further study the evolution of the UV–Vis spectra during the photo-oxidization reactions catalyzed by using $Fe_3O_4$ NPs, the spectral analysis was conducted in the visible light range (peak at 468.8 nm). Because the overlap of the frequency bands is so severe, the spectral parameters are accordingly highly correlated and the baseline is modulated, a rigorous regressions approach should be applied to achieve fitting convergence. Figure 7 a–h show the major peaks in the visible spectrum of the UV–Vis fitted to two skew bi-Gaussian peaks; the fitting
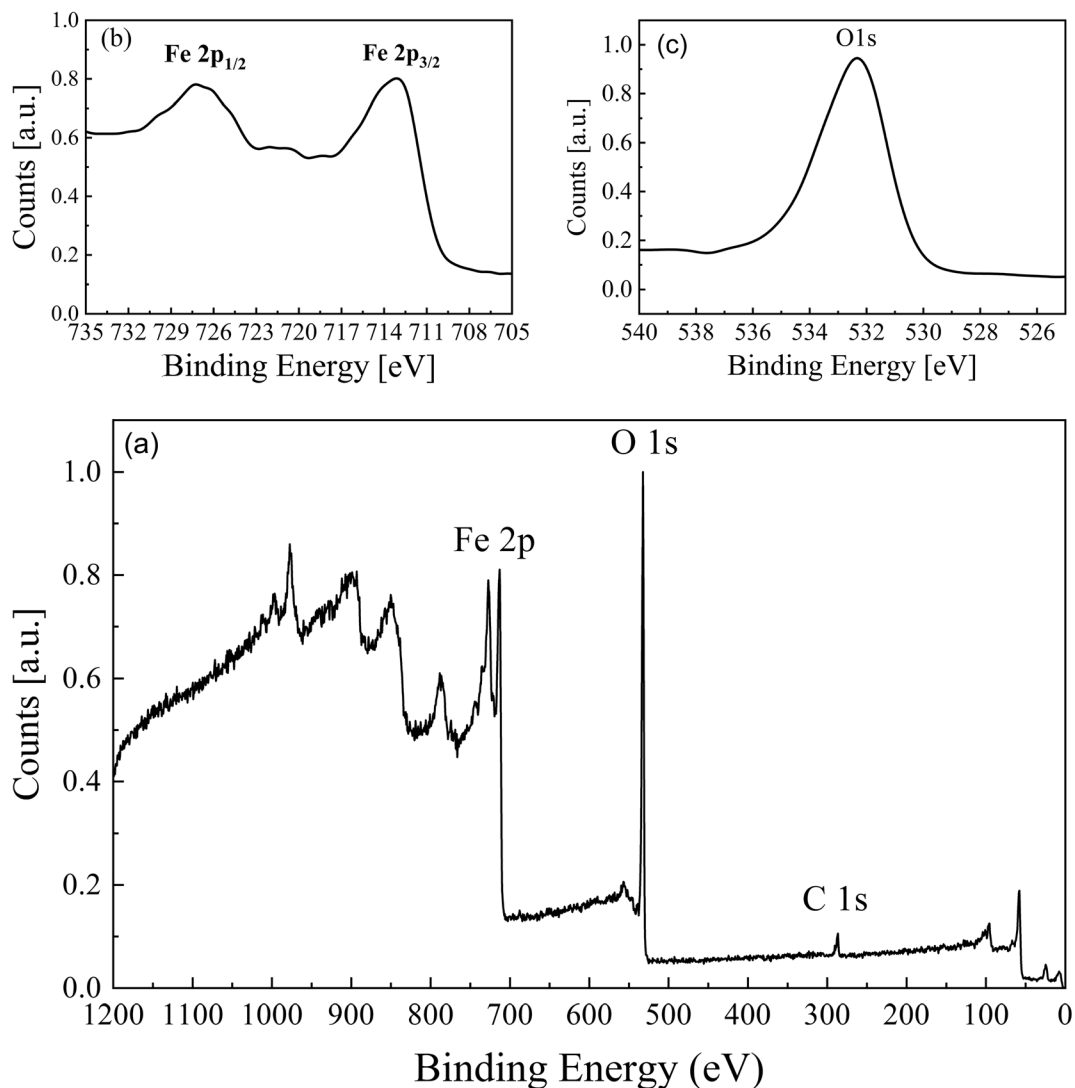
**Fig. 5** (a) XPS spectrum of the synthesized Fe$_3$O$_4$ NPs, (b) enlarged Fe 2p, and (c) O 1s peaks from the XPS spectrum in (a)

converted to the deconvoluted line describing adequately the experimental data. We likewise attempted the fitting of the absorbance maxima in the visible spectra with employing two Gaussian, Voigt, and log-normal distribution functions, but always obtained a much poorer fit than with the skewed bi-Gaussian function. The fitting quality when fitting to two peaks of skew bi-Gaussian was (based on the chi-square value) 18% better compared with fitting to two peaks of regular Gaussian peaks. Baseline correction and optimization algorithms and their parameter values for the UV–Vis spectra were done according to the algorithm described in (Li et al. 1993; Liland et al. 2010), in which the fit was found to be inadequate compared with other baseline algorithms such as polynomial or linear functions. Additionally, it was shown in the literature that an isolated frequency band corresponding to the $\pi > \pi^*$ transition for an azomethine dye as in the case of MO is best described by a skewed functions (Revers and Kaiser 1972).

All of the time-dependent absorption spectra exhibit two bands with maxima starting around 410 and 478 nm, with linewidths of 64 and 86 nm, respectively. The shape of the absorption spectrum was changing with irradiation time deduced from the progressing divergence of the two linewidth of the bi-Gaussian function. The peak position of the high-frequency component experienced an obvious blue shift of the absorption

Fig. 6 The acquired time evolution UV–Vis spectra of the MO during the photocatalytic degradation catalyzed by the synthesized $Fe_3O_4$ NPs at 0, 5, 10, 15, 20, 30, 40, 60, 80, 100, and 110 min
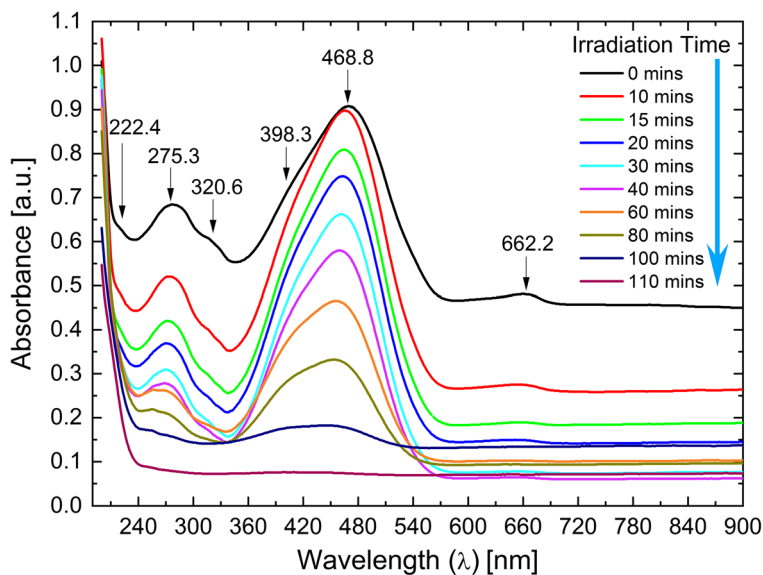


bands (Fig. 8c) until around 15 min of irradiation, indicating an increase of solvent polarity. This results in an initial hypsochromic shift in the MO absorbance maxima indicating that MO is behaving like hydrogen-bond acceptor (Özen et al. 2007). After continuous irradiation longer than 15 min, the higher frequency absorbance peak of the MO experiences a red shift, which means that the MO absorption ultimately shifts bathochromically. This indicates that MO is either playing a gradual role of a H-bond donor or the dissociated-intermediate products or MO are a H-bond donor (Reichardt 1994). The foregoing results suggest that unbonded hydroxyl is required to produce the large bathochromic shifts shown in Fig. 8c. Based on the above discussion along with relevant literature data, the bands of the major absorption peak can only be attributed to the H-bonded interaction between water and the azo nitrogens in the MO. The p-amino group enhances the basicity (see Fig. 10) of the azo nitrogen atoms (azonium ion of MO). The enhancement of basicity of –N=N by $Me_2N–$ was proven experimentally (see pH measurement in Fig. 10). Moreover, covalent protonation of the azo nitrogen atoms gives a pronounced red shift of the $\pi \rightarrow \pi*$ transition as we have discussed in the context of the bathochromical shift.

On further irradiation, a shallow bathochromic shift is seen and an asymptotic approach is expected, reflecting the nature of the process of MO decolonization and complete mineralization of the dye. Both bands were shifted in the identical pattern despite additional

difference in the absorbance-effected bonding indicating that the H-bond has influence on different sites of MO molecules.

The low-frequency component band experiences a monotonic continuity of bathochromic shifts and was best fitted to the BiDoseResp equation (using OriginLab), specifying the presence of two distinct equilibria (Ruzza et al. 2015) at configurations of hydrogen-bonding networks along with the MO dissociation during the photo-oxidation. The total absorbance maxima fitted only poorly to the same function indicating that the time-dependent degradation described by this total absorbance maxima is described by multiple processes. Therefore, studying the photo-oxidization evolving process and define its efficiency quantitatively relying on the as-measured overall absorbance maxima is not only inadequate but also misrepresentative. This is because the overall process is a complicated response to a combination of nonspecific and specific solute–solvent interactions, which are typical for the molecular chemical structure ability to conduct intermolecular interactions, dipole–dipole interaction, formation–disruption of hydrogen-bonding networks, and hydrophobic/hydrophilic interactions (Ababneh et al. 2018; Jensen et al. 2004). The same discussion can approximately be attributed to the amplitudes of the absorbance peaks evolution, and apparently, the integrated area under the peak is more appropriate to describe the overall process compared with the amplitude. Areas and amplitudes deduced individually from the
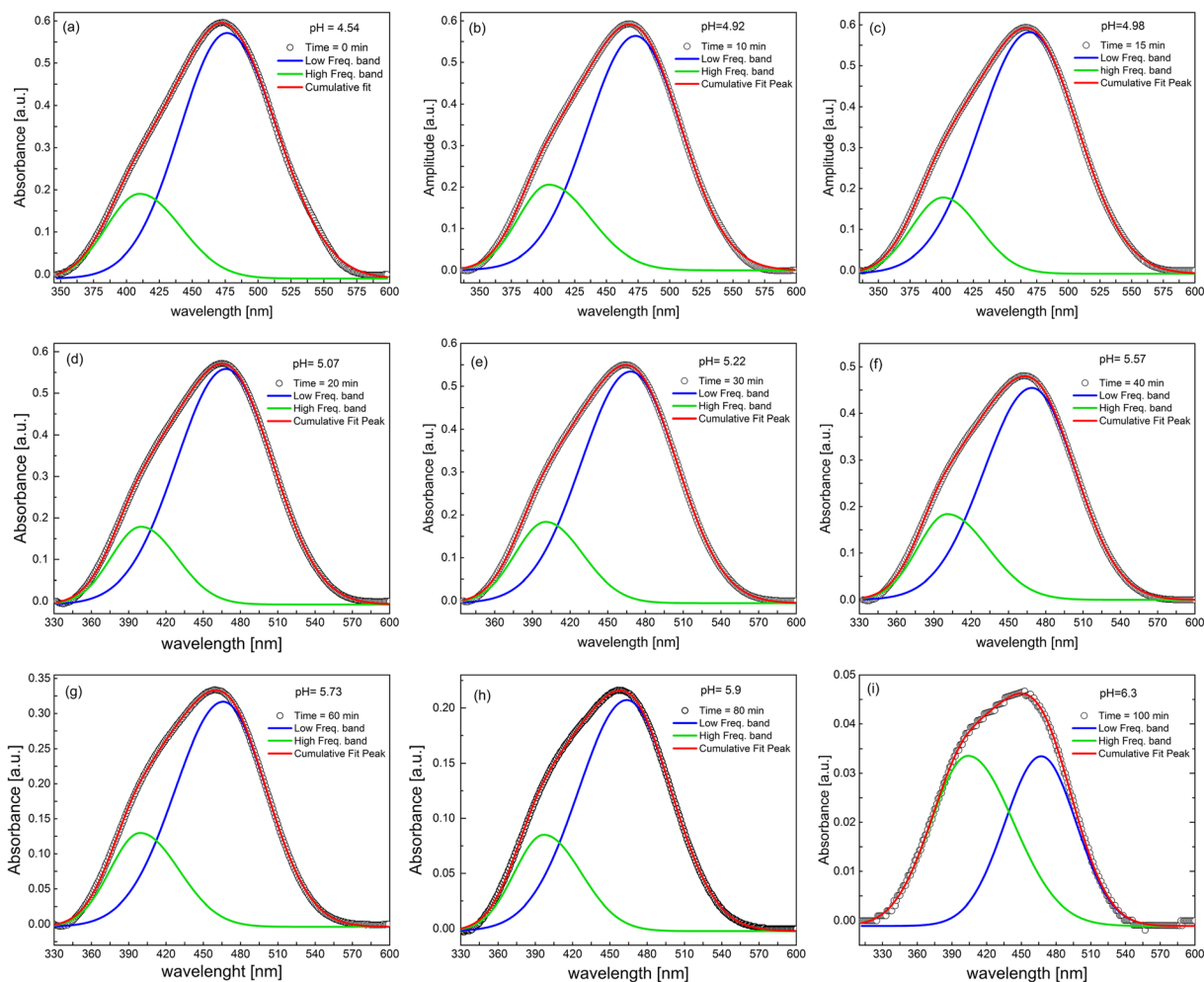
**Fig. 7** (**a–i**) Resolution of the UV–Vis absorption curves of MO for different UV irradiation time (0–100 min). The absorption lines have been fitted to two skewed bi-Gaussian peaks

low- and high-frequency bands as well as the overall absorbance maxima in Fig. 8a and b show initially similar trends correspondingly. The effect of the H-bond is dominantly seen in the high-frequency band of the visible spectrum. The most probable explanation is that during the photocatalytic degradation time, $H_2O$ and $O_2$ diffused in water capture the generated holes and electrons which results in •OH and superoxides ($•O_2^-$) radicals. The •OH and $•O_2^-$ radicals interact destructively with MO molecules resulting in decolorization of MO. The color of MO is determined by the azo bond (–N=N–) and its associated chromophores and auxochromes, where the energy difference between two separate molecular orbitals falls within the range of the visible spectrum (Bureš 2014), which is about 464 nm in

case of MO. The flat UV–Vis spectrum after 110 min indicates that MO molecules dissociate and are disrupted into smaller pieces. A continuous irradiation supports further oxidization of the dissociated smaller pieces of MO, until they are completely mineralized to $CO_2$, $H_2O$, $NO^-$, and $SO_2^-$.

Additional analysis of the UV–Vis spectra gives evidence of the existence of $FeCl_3 \cdot 6H_2O$ impurities based on assigning the shallow and broad absorbance peak found at 662.2 nm in the visible range. Typically, the ferric chloride hexahydrate ($FeCl_3 \cdot 6H_2O$) absorbance peaks appear at 296 and 590 nm (Bauer et al. 2005), whereas, in this work, these peaks appeared at around 320 and 662 nm, which probably belong to the ferric chloride hexahydrate ($FeCl_3 \cdot 6H_2O$) complexation with the $Fe_3O_4$.
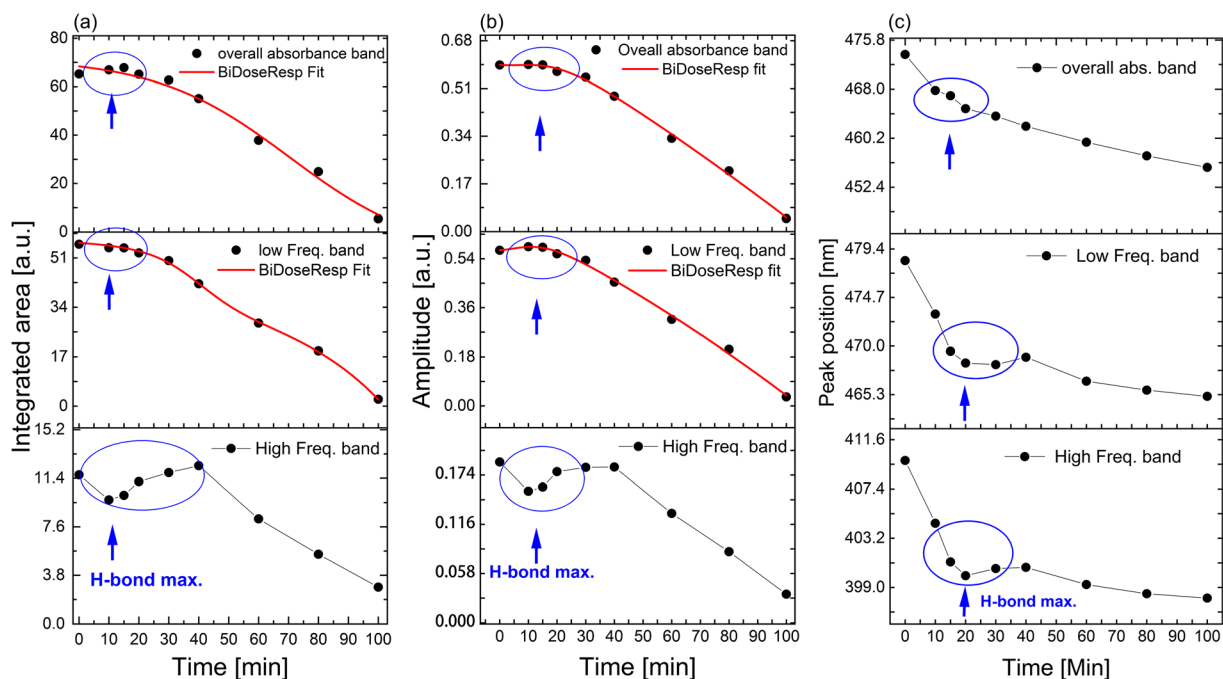
**Fig. 8** The analytical data deduced from the skewed bi-Gaussian fitting (Fig. 6) of the time-dependent UV–Vis spectra in Fig. 5 (a). The area, (b) the amplitude, and the (c) peak position of the low, high, and convoluted frequency bands. The acidity (pH) of the solution was not controlled and defined according to the oxidization conditions. The straight lines between the data points just serve to guide the eye

Interestingly, UV–Vis spectra offer the possibility to identify bis- and tris-diketonato–Fe(III) compounds in protic solution (MO–$Fe_3O_4$–$H_2O$ in this study) based on the characteristic absorbance peak positions which occurred in the obtained result of this work at $\lambda > 600$ nm (see Fig. 6) and it is in agreement with literature (Barreca et al. 2012; Handa et al. 1992).



**Fig. 9** Electrical conductivity ($\sigma$) evolution of the MO solution during the photocatalytic degradation time by using the synthesized $Fe_3O_4$ NPs as a photocatalytic. The red line is the bi-exponential decay fit
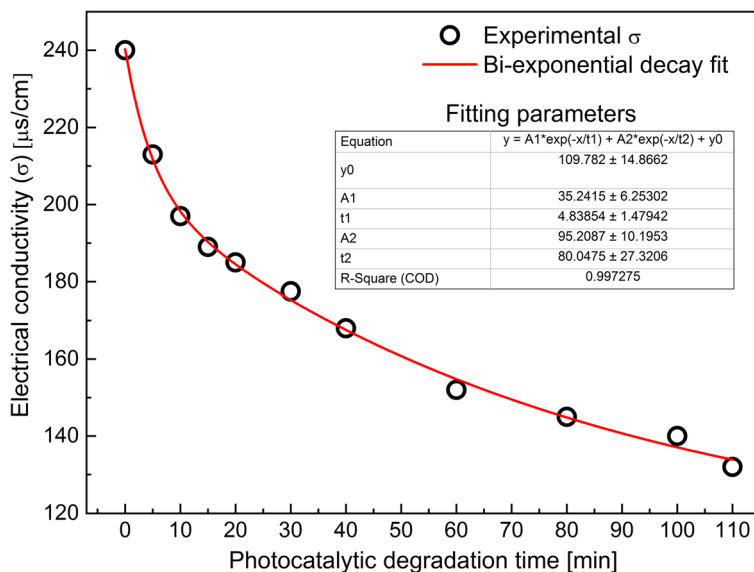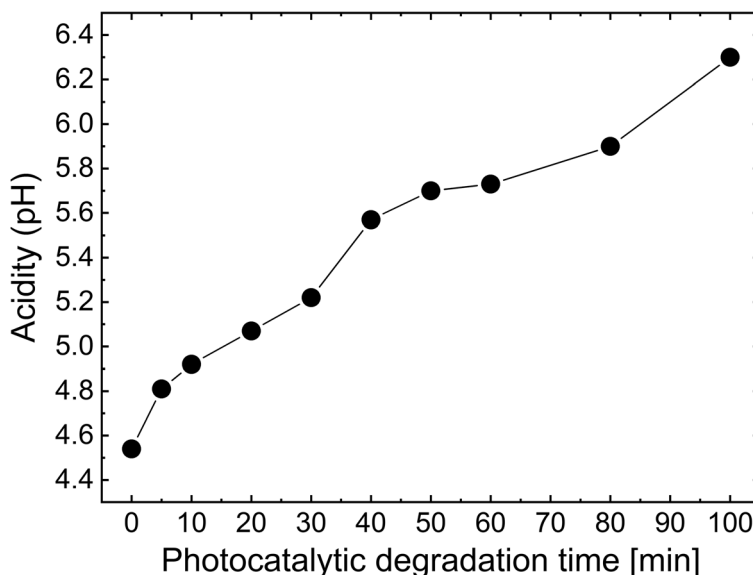
**Fig. 10** The acidity (pH) evolution of the MO solution during the photocatalytic degradation time by using the synthesized $Fe_3O_4$ NPs as a photocatalytic. Straight line connecting the experimental points serves as a guide for the eye



## 3.3 Electrical Conductivity ($\sigma$) and the Acidity (pH) Evolvement

The time-dependent variations of the electrical conductivity ($\sigma$) and the pH of the MO solution catalyzed with $Fe_3O_4$ NP are plotted in Figs. 9 and 10, respectively. The electrical conductivity dropped from 240 to 132 $\mu$s/cm at the end of the photocatalytic degradation process. The multi-exponential decrease of the electrical conductivity versus the oxidization/degradation time cannot be explained only by an inhibition of inorganic ions (like $Na^+$). This finding emphasizes that the electrical conductivity is a combined processes of the inhibition of inorganic ions and the attenuation of the H-bonding network.

The time-dependent electrical conductivity of the MO in the protic solution was best fitted to a bi-exponential decay function, showing two dynamic processes. One is a dominant process that contributes 20-fold more than a second process to the overall electrical conductivity. Most probably, the minor contribution refers to the inhibition of inorganic ions such as the dissociated $Na^+$ from the MO. The major contribution refers to the hydrogen-bonded network dynamics and/or hydrophobic/hydrophilic interactions. The dynamics of the major contribution is due to the dissociation of MO into smaller pieces and eventually the mineralization of the small pieces into $CO_2$, $H_2O$, $NO^-$, and $SO_2^-$ (Reeves et al. 1973). Additionally, the electrical conductivity is facilitated by the tautomerization since the methyl

orange is an azo dye, with a pKa value of 3.5 that has a basic and two acidic forms (Carrazana et al. 2004). The effect of tautomerization is somewhat correlated to the H-bonding network. For this reason, we considered the effect of tautomerization being embedded in the major contributor and hence, the electrical conductivity cannot be described only by inhibition of inorganic ions.

The significant change of the acidity of the solution as it is depicted in Fig. 10 is a second proof of the effect of the H-bonded network, since the inhabitance of the inorganic ions such as $Na^+$ will not cause such a pronounced change of acidity. Because of the hydrogen-bonding network evolution, the hydroxyl radicals and/or the hydronium ions are generated accordingly (Karimi et al. 2014).

The acidity of the treated MO can be controlled to sustain a high degradation efficiency: degradation of organic molecules is suppressed at high pH values (pH > 12) due to the competitive adsorption of hydroxyl ions with organic molecules on the surface of the catalysts (Chiang and Lin 2013).

## 3.4 Photocatalytic Degradation Kinetics of MO

Photocatalytic degradation experimental data of MO solution by using $Fe_3O_4$ NPs is plotted in Fig. 11. The general equation describing the reaction rate and the integral form of the concentration profile can be described according to Eqs. (1) and (2), respectively.

$$-dC/dt = k\, C^n \qquad (1)$$

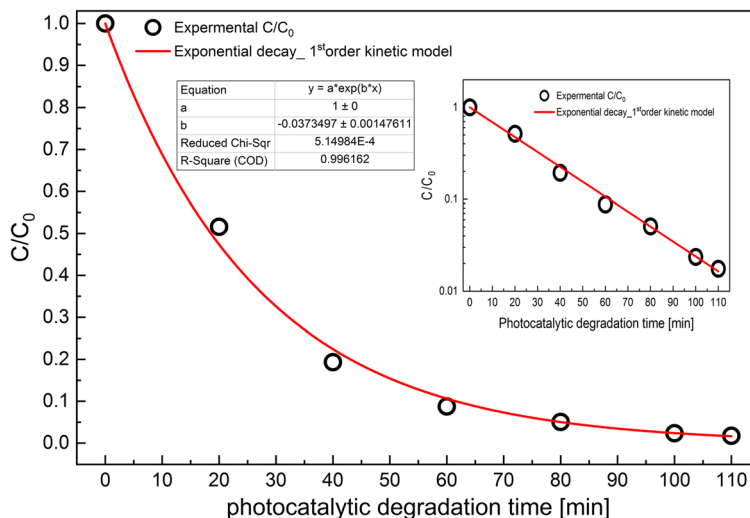$$1/C^{(n-1)} = 1/C_o^{(n-1)} + (n-1)\, k\, t \qquad (2)$$

where $C_o$ and $C$ are the initial concentration and the progressive concentration of MO in mg/L, respectively; $t$ is the contact time in minutes; and $k$ and $n$ are the kinetics parameters. The experimental data have been fitted to the pseudo-first-order kinetic model where the kinetics of MO degradation was investigated using the integral method (Chiha et al. 2010). The best correlation coefficient ($R^2$) which was used to find the fitting is 0.9961 and the rate constant, $k$, is around 0.037 min$^{-1}$.

The MO initial concentration was 1175 ppm and is based on Fig. 11; the photocatalytic efficiency of $Fe_3O_4$ nanoparticles is 98.3% in 110-min irradiation time.

The decolorization efficiency of MO catalyzed with $Fe_3O_4$ deduced from the visible branch of the UV–Vis spectra is plotted in Fig. 12. Both amplitude and area (Fig. 8) are shown for the lower frequency band as well as the overall convoluted absorbance band. The deduced efficiencies from the overall absorbance maxima and from the low-frequency band have a discrepancy of 50.1% at 20 min and 12.3% at 60 min representing the progressive attenuation of the H-bonds impact due to the dissociation of MO (decolorization).

H-bonds are considered weak since their energies are in the range of 3 to 7 kcal mol$^{-1}$ and they keep the proton in a double-well potential. Once the atoms (involved in the H-bonds) come closer to each other,

the potential barrier becomes lower (stronger H-bonds) and finally disappears, leading to a single-well potential (Kreevoy and Liang 1980). To conclude, when the potential barrier between the double well is non-existent, the H-bond becomes substantially strong (Cleland and Kreevoy 1994) which is quantitatively different from normal H-bonds and has been proven by X-ray crystallography (Hibbert and Emsley 1990). The equilibrium constants for the formation of H-bonded complexes such as MO–MO$^-$ are higher than in pure water. H-bonded complex formation is so weak in water that it is difficult to measure the equilibrium constants which is very clear in Fig. 12b where the deviation between the low-frequency band and the overall absorbance maxima are at the maximum. During the photodegradation process, H-bonded complexation of MO–MO$^-$ is reduced throughout the degradation and mineralization of MO. Simultaneously (see Fig. 12b), the deviation between the low-frequency band and the overall absorbance maxima decreases gradually.

The obtained results show a significant enhancement of MO degradation, using $Fe_3O_4$ NPs catalysis, compared with conditions used by other scientists. For example, the photocatalytic degradation efficiency of MO (initial COD 1175 mg/L) in this study has been compared with those obtained by Pacheco-Álvarez et al. (Pacheco-Álvarez et al. 2018b). The measurement with initial COD 140 mg/L and under different advanced oxidation processes that include (i) electrolysis using BDD anode, (ii) electro-oxidation using $TiO_2$/BDD, (iii) photoelectro-oxidation using $TiO_2$/BDD/hv showed a poorer



**Fig. 11** The ratio $C/C_0$ of MO as a function of photocatalytic degradation time fitted to the first-order kinetic model represented by the solid red line. The inset is the same plot but scaling $y$ with logarithmic scale in order to show the quality of the linearity dependent of the experimental data to the first-order kinetic model. Fitting parameters are included

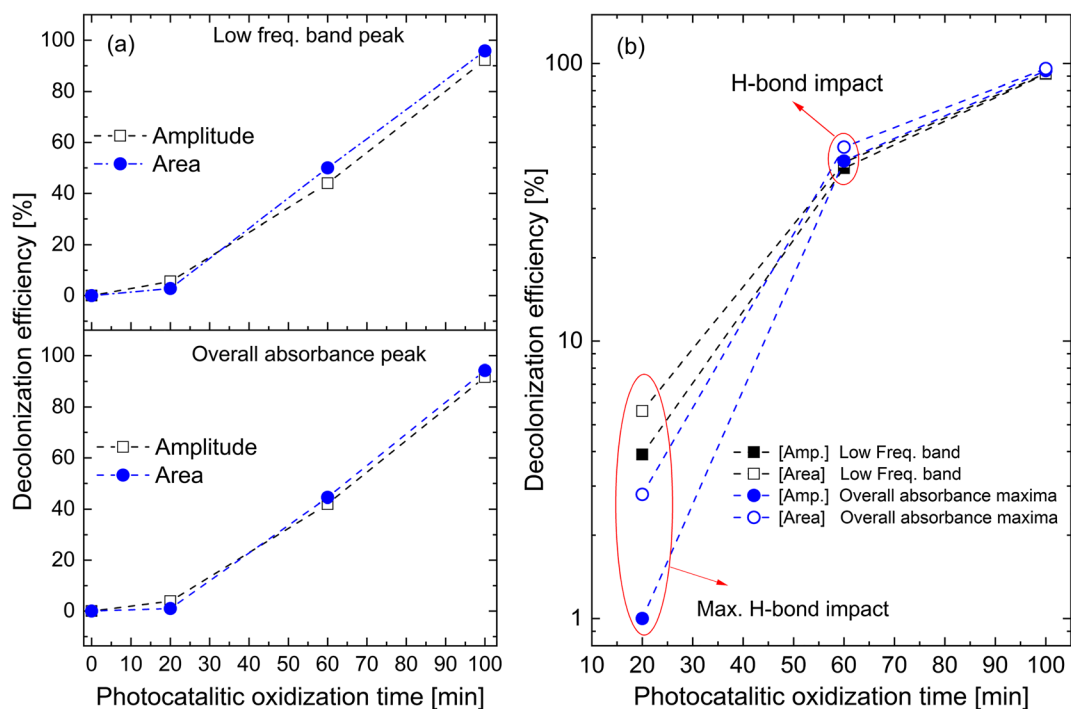| Equation | y = a*exp(b*x) |
|---|---|
| a | 1 ± 0 |
| b | -0.0373497 ± 0.00147611 |
| Reduced Chi-Sqr | 5.14984E-4 |
| R-Square (COD) | 0.996162 |

**Fig. 12** The time evolution of the decolorization efficiency of MO based on amplitude and area of **a** the overall absorbance maxima and the low-frequency band plotted separately and in linear scale, and **b** for comparison in semi-logarithmic scale

performance compared with the work in this study (Table 1).

Only 61% degradation of MO was obtained within 110 min of treatment time compared with 70% obtained under electro-oxidation. In addition, the photoelectro-oxidation results in only 89% degradation versus 98.3% based on photocatalytic oxidation using $Fe_3O_4$ after 110 min of treatment.

## 4 Summary and Conclusions

$Fe_3O_4$ nanoparticles (NPs) have been synthesized using the coprecipitation method as a catalytic agent for the photodegradation of methyl orange (MO) dye for removal from water. The average crystallite sizes of the synthesized $Fe_3O_4$ NPs was calculated by the Scherrer equation using the average of all XRD peaks and the average size was 28 nm which is in good agreement with relevant reported literature for $Fe_3O_4$ NPs. The results were augmented by calculating the average size distributions statically from SEM micrographs and were found to be around 31.5 nm.

Strong peaks assigned to Fe and O atoms are observed in the EDAX spectrum with weight percentages of 81.84% and 17.32% respectively. In addition, traces of Cl as impurities remaining from the synthesis of about 0.84% have been determined.

In the XPS spectrum, the presence of satellite peaks around 719 eV, which are characteristic of $Fe_2O_3$ phases, confirms the presence of only $Fe^{3+}$ species in the NPs lattice emphasizing the presence dominantly of a $Fe_3O_4$ structural phase form.

The UV–Vis maxima consist of more than a single absorption peak (frequency band) which derives from the fact that an obvious shoulder is seen on the high-frequency side (around 398.3 nm) of the absorbance curve. A significant and non-monotonic spectral dynamic including peak wavelength shifts, absolute amplitude, and area changes for the band of MO and probably for $Fe_3O_4$/MO complexes suggest that the cleavage of the azo bond is not the only and/or the dominant process in the photocatalytic oxidization of the MO in protic solution. The peaks in the visible spectrum of the UV–Vis response were fitted to two skew bi-Gaussian peaks that was 18% better compared with

**Table 1** Comparison of chemical oxygen demands (COD) removal obtained in our study with those obtained from various advanced oxidation processes

| Advance oxidation treatment method | Initial COD (mg/L) | Removal (%) |
|---|---|---|
| Electrolysis using BDD anode | 140 | 61 |
| Electro-oxidation using $TiO_2$/BDD | 140 | 70 |
| Photoelectro-oxidation using $TiO_2$/BDD/hv | 140 | 89 |
| Photocatalytic oxidation using $Fe_3O_4$ | 1180 | 98 |

a fit to two regular Gaussian peaks. Subsequently, fitting of an isolated frequency band corresponding to the $\pi > \pi^*$ transition for an azomethine dye as in the case of MO is best described by a skewed function. The high-frequency band is best assigned to a hydrogen-bonded interaction between water and the azo nitrogens in the MO.

Judging the evolution of the photo-oxidization process and quantifying its efficiency based on the as-measured overall absorbance maxima are not only inadequate but also misrepresentative: the overall process is a complicated response to a combination of nonspecific and specific solute/solvent interactions. Additionally, this response is typical for the molecular chemical structure ability to record intermolecular interactions, dipole/dipole interactions, generation/disruption of hydrogen-bonding networks, and hydrophobic/hydrophilic interactions.

A bi-exponential decay is the best fitting function to describe the decay of the time-dependent electrical conductivity of the MO–water solution under photocatalytic oxidization. The fit shows that the dominant process assigned to the hydrogen-bonded network dynamics and/or hydrophobic/hydrophilic interactions has a contribution of around 20-fold of the minor process that is attributed to the inhibition of inorganic ions such as the dissociated $Na^+$ from MO.

The COD process is best described by a pseudo-first-order model. The efficiency of the process is 98.3% in 110-min irradiation time taking into account the initial concentration of 1175 ppm of MO. The decolorization efficiency (98.3%) deduced from the peak integration of the low-frequency band is in agreement with that deduced from the amplitude of the same peak at the end of the degradation process (after 110 min). This is because the impact of the H-bonding between the MO, $MO^-$, and the buffer solution is at the minimum, supporting the proposed hypothesis of this work. The deduced efficiencies from the overall absorbance maxima and

from the low-frequency band, however, have a discrepancy of 50.1% at 20 min and 12.3% at 60 min representing the progressive attenuation of the H-bond impact due to the dissociation of MO (decolorization).

The obtained results show significant enhancement of MO degradation using $Fe_3O_4$ NPs catalysis as compared with conditions used by other scientists. Thus, the $Fe_3O_4$ nanoparticles can be expansively applied in several industrial water treatment applications for organic contaminant removal.

## References

Ababneh, R., Telfah, A., Jum'h, I., Abudayah, M., Al-Abdallat, Y., Lambert, J., & Hergenröder, R. (2018). ^{1}H NMR spectroscopy to investigate the kinetics and the mechanism of proton charge carriers ionization and transportation in hydrophilic/hydrophobic media: methyl sulfonic acid as a protonic ion source in water/alcohol binary mixtures. *Journal of Molecular Liquids, 265*, 621–628.

Alavi, S., Takeya, S., Ohmura, R., Woo, T. K., & Ripmeester, J. A. (2010). Hydrogen-bonding alcohol-water interactions in binary ethanol, 1-propanol, and 2 propanol+methane structure II clathrate hydrates. *The Journal of Chemical Physics, 133.*

Ali, A., Hira Zafar, M. Z., Ul Haq, I., Phull, A. R., Ali, J. S., & Hussain, A. (2016). Synthesis, characterization, applications, and challenges of iron oxide nanoparticles. *Nanotechnology, Science and Applications, 9*, 49.

Alinsafi, A., Evenou, F., Abdulkarim, E. M., Pons, M. N., Zahraa, O., Benhammou, A., Yaacoubi, A., & Nejmeddine, A. (2007). Treatment of textile industry wastewater by supported photocatalysis. *Dyes and Pigments, 74*, 439–445.

Alqaradawi, S., & Salman, S. (2002). Photocatalytic degradation of methyl orange as a model compound. *Journal of Photochemistry and Photobiology A: Chemistry, 148,* 161–168.

Andrade, A. L., Fabris, J., Ardisson, J., Valente, M. A., & Ferreira, J. M. F. (2012). Effect of tetramethylammonium hydroxide on nucleation, surface modification and growth of magnetic nanoparticles. *Journal of Nanomaterials, 454,* 759.

Bagbi, Y., Sarswat, A., Mohan, D., Pandey, A., & Solanki, P. R. (2017). Lead and chromium adsorption from water using L-cysteine functionalized magnetite (Fe3O4) nanoparticles. *Scientific Reports, 7,* 7672.

Barbosa, A., Bonifácio, L., & Dias, S. (2018). Wastewater reuse: case study of Abrunheira's Industrial Water Treatment Plant, *Modeling Innovation Sustainability and Technologies* (pp. 311–317). Online ISBN 978–3–319-67,101-7.

Barreca, D., Carraro, G., Devi, A., Fois, E., Gasparotto, A., Seraglia, R., Maccato, C., Sada, C., Tabacchi, G., Tondello, E., Venzo, A., & Winter, M. (2012). β-Fe$_2$O$_3$ nanomaterials from an iron(II) diketonate-diamine complex: a study from molecular precursor to growth process. *Dalton Transactions, 41,* 149.

Bauer, M., Kauf, T., Christoffers, J., & Bertagnolli, H. (2005). Investigations into the metal species of the homogeneous iron(III) catalyzed Michael addition reaction. *Physical Chemistry Chemical Physics, 7,* 2664–2670.

Bureš, F. (2014). Fundamental aspects of property tuning in push–pull molecules. *RSC Advances, 4,* 58,826–58,851.

Carrazana, J., Reija, B., Ramos Cabrer, P., Al-Soufi, W., Novo, M., & Tato, J. V. (2004). Complexation of methyl orange with b-cyclodextrin: detailed analysis and application to quantification of polymer-bound cyclodextrin. *Supramolecular Chemistry, 16,* 549–559.

Chandler, D. (2005). Interfaces and the driving force of hydrophobic assembly. *Nature, 437,* 640–647.

Chiang, Y., & Lin, C. (2013). *Powder Technology, 246,* 137.

Chiha, M., Merouani, S., Hamdaoui, O., Baup, S., Gondrexon, N., & Pétrier, C. (2010). *Ultrasonics Sonochemistry, 17,* 773.

Cleland, W., & Kreevoy, M. (1994). Low-barrier hydrogen bonds an enzymic catalysis. *Science, 264,* 1887–1890.

Dagher, S., Soliman, A., Ziout, A., Tit, N., Hilal-Alnaqbi, A., Khashan, S., Alnaimat, F., & Qudeiri, J. (2018). *Materials Research Express., 5,* 065518.

Dannenberg, J. J. (2002). Cooperativity in hydrogen bonded aggregates. Models for crystals and peptides. *Journal of Molecular Structure, 615,* 219–226.

Eisenberg, D., & Kauzmann, W. (1969). *The structure and properties of water.* Oxford: Oxford University Press.

El Ghandoor, H., Zidan, H. M., Mostafa, M. H., & Khalil, M. I. M. I. (2012). Synthesis and some physical properties of magnetite (Fe$_3$O$_4$) nanoparticles. *International Journal of Electrochemical Science, 7,* 5734–5745.

Fujii, T., de Groot, F. M. F., Sawatzky, G. A., Voogt, F. C., Hibma, T., & Okada, K. (1999). *Physical Review B: Condensed Matter and Materials Physics, 59,* 3195.

Genuino, H., Mazrui, N., Seraji, M., Luo, Z., & Hoag, G. (2013). Green synthesis of iron nanomaterials for oxidative catalysis of organic environmental pollutants. In *New and Future Developments in Catalysis. Catalysis for Remediation and Environmental Concerns* (1st ed., pp. 41–61). Amsterdam: Elsevier.

Guerra, F. D., Campbell, M. L., Whitehead, D. C., & Alexis, F. (2017). Tunable properties of functional nanoparticles for efficient capture of VOCs. *ChemistrySelect., 2,* 9889–9894.

Guo, H., Stan, G., & Liu, Y. (2018). *Soft Matter, 14,* 1311.

Gutierrez, A. M., Dziubla, T. D., & Hilt, J. Z. (2017). Recent advances on iron oxide magnetic nanoparticles as sorbents of organic pollutants in water and wastewater treatment. *Reviews on Environmental Health, 32,* 111–117.

Handa, M., Miyamoto, H., Suzuki, T., Sawada, K., & Yukawa, Y. (1992). Solvent effects on acetylacetonato iron complexes. *Inorganica Chimica Acta, 203,* 61.

Heidari, A., Mir, N., & Nikkaran, A. R. (2016). Phenylalanine removal from water by Fe3O4 nanoparticles functionalized with two different surfactants. *J Nanostructures, 6*(3), 199–206.

Hibbert, F., & Emsley, J. (1990). Hydrogen bonding and chemical reactivity. *Advances in Physical Organic Chemistry, 26,* 255–379.

Ibrahim Dar, M., & Shivashankar, S. A. (2014). Single crystalline magnetite, maghemite, and hematite nanoparticles with rich coercivity. *RSC Advances, 4,* 4105.

Jang, S., Hira, S. A., Annas, D., Song, S., Yusuf, M., Park, J. C., Park, S., & Park, K. H. (2019). Recent novel hybrid Pd–Fe$_3$O$_4$ nanoparticles as catalysts for various C–C coupling reactions. *Processes, 7,* 422.

Jensen, M. Ø., Mouritsen, O. G., & Peters, G. H. (2004). The hydrophobic effect: molecular dynamics simulations of water confined between extended hydrophobic and hydrophilic surfaces. *The Journal of Chemical Physics, 120,* 9729–9744.

Jum'h, I., Abdelhay, A., Al-Taani, H., Telfah, A., Alnaief, M., & Rosiwal, S. (2017a). Fabrication and application of boron doped diamond BDD electrode in olive mill wastewater treatment in Jordan. *Journal of Water Reuse and Desalination., 7,* 502.

Jum'h, I., Telfah, A., Lambert, J., Gogiashvili, M., Al-Taani, H., & Hergenröder, R. (2017b). $^{13}$C and $^{1}$H NMR measurements to investigate the kinetics and the mechanism of acetic acid (CH$_3$CO$_2$H) ionization as a model for organic acid dissociation dynamics for polymeric membrane water filtration. *Journal of Molecular Liquids, 227,* 106–113.

Karimi, L., Zohoori, S., & Yazdanshenas, M. E. (2014). Photocatalytic degradation of azo dyes in aqueous solutions under UV irradiation using nano-strontium titanate as the nanophotocatalyst. *Journal of Saudi Chemical Society, 18*(5), 581–588.

Kreevoy, M. M., & Liang, T. M. (1980). Structures and isotopic fractionation factors of complexes, A1HA-2. *Journal of the American Chemical Society, 102,* 3315–3322.

Laage, D., & Hynes, J. T. (2006). Do more strongly hydrogen-bonded water molecules reorient more slowly? *Chemical Physics Letters, 433,* 80–85.

Lacroix, L.-M., Delpech, F., Nayral, C., Lachaize, S., & Chaudret, B. (2013). New generation of magnetic and luminescent nanoparticles for in vivo real-time imaging. *Interface Focus, 3,* 1–19.

Lau, Y. Y., Wong, Y. S., Teng, T. T., Morad, N., Rafatullah, M., & Ong, S. A. (2015). Degradation of cationic and anionic dyes in coagulation–flocculation process using bi-functionalized silica hybrid with aluminum-ferric as auxiliary agent. *RSC Advances, 5,* 34,206–34,215.

Legrini, O., Oliveros, E., & Braun, A. (1993). Photochemical processes for water treatment. *Chemical Reviews, 93*, 671.

Li, X., Zhang, Z., & Henrich, V. E. (1993). Inelastic electron background function for ultraviolet photoelectron spectra. *Journal of Electron Spectroscopy and Related Phenomena, 63*, 253–265.

Liland, K., Almøy, T., & Mevik, B.-H. (2010). Optimal choice of baseline correction for multivariate calibration of spectra. *Applied Spectroscopy, 64*, 1007–1016.

Lopez, J., González, F., Bonilla, F., Zambrano, G., & Gómez, M. (2010). *RevistaLatinoamericana de Metalurgia y Materiales., 30*, 60.

Lops, C., Ancona, A., Di Cesare, K., Dumontel, B., Garino, N., Canavese, G., Hérnandez, S., & Cauda, V. (2019). Sonophotocatalytic degradation mechanisms of rhodamine B dye via radicals generation by micro- and nano-particles of ZnO. *Applied Catalysis. B, Environmental, 243*, 629–640.

Mascolo, M. C., Pei, Y., & Ring, T. A. (2013). Room temperature co-precipitation synthesis of magnetite nanoparticles in a large pH window with different bases. *Materials (Basel)., 6*, 5549–5567.

Mortazavian, S., Saber, A., & James, D. E. (2019). Optimization of photocatalytic degradation of acid blue 113 dye and acid red 88 textile dyes in UV-C/TiO2 suspension system: application of response surface methodology (RSM). *Catal, 9*, 1–19.

Namanga, J., Foba, J., Ndinteh, D. T., Yufanyi, D. M., & Krause, R. W. M. (2013, 2013). Synthesis and magnetic properties of a superparamagnetic nanocomposite "Pectin-Magnetite Nanocomposite". *Journal of Nanomaterials*, 137275, 8 pages.

Nançoz, C., Licari, G., Beckwith, J. S., Soederberg, M., Dereka, B., Rosspeintner, A., Yushchenko, O., Letrun, R., Richert, S., Lang, B., & Vauthey, E. (2018). *Physical Chemistry Chemical Physics, 20*, 7254–7264.

Nardo, L., Paderno, R., Andreoni, A., Másson, M., Haukvik, T., & Tønnesen, H. H. (2008). Role of H-bond formation in the photoreactivity of curcumin. *Spectroscopy, 22*, 187–198.

Özen, A. S., Doruker, P., & Aviyente, V. (2007). Effect of cooperative hydrogen bonding in azo−hydrazone tautomerism of azo dyes. *The Journal of Physical Chemistry A, 111*, 51 13, 506–13,514.

Pacheco-Álvarez, M., Rodríguez-Narváez, O., Wrobel, K., Navarro-Mendoza, R., Nava-Montes de Oca, J., & Peralta-Hernández, J. (2018a). Improvement of the Degradation of Methyl Orange Using a TiO2/BDD Composite Electrode to Promote Electrochemical and Photoelectro-Oxidation Processes. *Int. J. Electrochem. Sci., 13*, 11549–11567.

Pacheco-Álvarez, M., Rodríguez-Narváez, O., Wrobel, K., Navarro-Mendoza, R., Nava-Montes de Oca, J., & Peralta-Hernández, J. (2018b). *International Journal of Electrochemical Science, 13*, 11,549.

Park, H., Ayala, P., Deshusses, M., Mulchandani, A., Choi, H., & Myung, N. (2008). Electrodeposition of maghemite (γ-Fe2O3) nanoparticles. *Chemical Engineering Journal, 139*, 208.

Reeves, R. L., Kaiser, R. S., Maggio, M. S., Sylvestre, E. A., & Lawton, W. H. (1973). Analysis of the visual spectrum of methyl orange in solvents and in hydrophobic binding sites. *Canadian Journal of Chemistry, 51*(4), 628–635.

Reichardt, C. (1994). Solvatochromic dyes as solvent polarity indicators. *Chemical Reviews, 94*, 2319–2358.

Revers, R. L., & Kaiser, R. S. (1972). In H. H. G. Jel-linek (Ed.), *Water structure at the water-polymer interface* (p. 56). New York: Plenum Press.

Rizzo, L., Malato, S., Antakyali, D., Beretsou, V. G., Đolić, M. B., Gernjak, W., Heath, E., Ivancev-Tumbas, I., Karaolia, P., & Ribeiro, A. R. L. (2019). Consolidated vs new advanced treatment methods for the removal of contaminants of emerging concern from urban wastewater. *Science of the Total Environment, 655*, 986–1008.

Ruzza, P., Hussain, R., Biondi, B., Calderan, A., Tessari, I., Bubacco, L., & Siligardi, G. (**2015**). Effects of trehalose on thermodynamic properties of alpha-synuclein revealed through synchrotron radiation circular dichroism. *Biomolecules, 5*, 724–734.

Sauer, T., Neto, G., Jose, H., & Moreira, R. (2002). *Journal of Photochemistry and Photobiology A: Chemistry, 149*, 147.

Silva, A., Santos, L. H. M. L. M., Antão, C., Delerue-Matos, C., & Figueiredo, S. A. (2017). Ecotoxicological evaluation of chemical indicator substances present as micropollutants in laboratory wastewaters. *Global NEST Journal, 19*, 94–99.

Sun, S., & Zheng, H. (2002). Size-controlled synthesis of magnetite nanoparticles. *Journal of the American Chemical Society, 124*, 8204–8205.

Tzitzi, M., Vayenas, D. V., & Lyberatos, G. (1994). Pretreatment of textile industry wastewaters with ozone. *Water Science and Technology, 29*, 151–160.

Wu, S., Sun, A., Zhai, F., Wang, J., Xu, W., Zhang, Q., & Volinsky, A. (2011). Fe3O4 magnetic nanoparticles synthesis from tailings by ultrasonic chemical co-precipitation. *Materials Letters, 651*, 882.

Xin, X., Wei, Q., Yang, B. J., Yan, L., Feng, R., Chen, G., Du, B., & Li, H. (2012). Highly efficient removal of heavy metal ions by amine-functionalized mesoporous Fe3O4 nanoparticles. *Chemical Engineering Journal, 184*, 132–140.

Yaseen, D. A., & Scholz, M. (2019). Textile dye wastewater characteristics and constituents of synthetic effluents: a critical review. *International Journal of Environmental Science and Technology, 16*, 1193.

Zysler, R., Mansilla, M., & Fiorani, D. (2004). Surface effects in α-Fe2O3 nanoparticles. *The European Physical Journal B-Condensed Matter and Complex Systems, 41*, 171.